### 6) Synthesis of ZSM-5

ZSM-5 was synthesized in a wide variety of systems to fulfill three main objectives. The first objective was to prepare ZSM-5 catalysts having a wide variety of silica to alumina ratios. As previously discussed, the higher the concentration of aluminum in the framework the more polar is its nature. These catalysts were needed by Pittsburgh Energy Technology Center to investigate the Bronsted and Lewis acidity by IR techniques and to investigate the effect of silica ratio on the product formed by bifunctional iron and cobalt thoria ZSM-5 catalysts. The syntheses were carried out at autogenous pressure in non-stirred Parr autoclaves. A summary Table of the synthesis runs carried out varying silica to alumina ratio for 10:1 to 150:1 is given in Table 26 of appendix D.

The second objective was to vary the morphology and increase the size of the ZSM-5 crystals. The exploratory runs carried out are summarized in Table 27 of Appendix D. Buffering the pH of the hydrothermal magma and stabilizing the silica precursors with ammonia resulted in the formation of ZSM-5 crystals 100 microns in size. Examples of the various crystal morphologies obtained in systems containing ammonia are shown in Figure 91 and in Figures 78 a,b,c,d. The spherical crystals in Figure 78 c were formed in run number DOD-8 (see appendix D). The fluidized crystals shown in Figures 78a and b were formed in the Parr autoclave at

180 C from a batch composition 4 $TPA_2O$ $8(NH_4)_2O \cdot 1Al_2O_3 \cdot 60\ SiO_2 \cdot 750\ H_2O$. As these crystals are in the fluidizable size range, they are likely to be useful in fluid bed reactors for processes such as Mobil's fluidized MTG process. The crystals shown in Figure 78 d were formed in the Parr autoclave using a batch composition $8TPA_2O$ $38(NH_4)_2O \cdot 1Al_2O_3 \cdot 60\ SiO_2 \cdot 750\ H_2O$ at 180 C. In systems such as this containing large concentrations of ammonium hydroxide, care must be taken to avoid the dangerously high pressures which can develop if the reactor over-shoots its temperature set point during the heat-up process. The large crystals formed were found to be valuable in determining the extent of metal transport into the ZSM-5 pore system during metal loading. The incipient wetness, aqueous iron nitrate impregnation of the large ZSM-5 crystals shown in Figure 91 are shown in Figures 92 a,b,c,e,f. Figure 92 d is a back scatter electron image showing the location of iron atoms in the crust-like material coating the crystal in Figure 92c. To look for metal concentrations within the zeolite crystals the following procedure was undertaken.

Following metal impregnation, the crystals were coated with gold three times using a gold sputtering device. The crystals were then fractured between 2 glass slides and mounted on carbon. Energy dispersive electron microprobe analysis was then performed at various locations on the fractured surface of the ZSM-5 crystals. The absence of the gold peak indicated that the surface was fractured after and not before the metal loading. Figures 93 a through f show two fractured ZSM-5 crystals which had been impregnated with cobalt thoria. The surfaces shown in Figures 93 a,c,e were analyzed at the locations shown in Figures 93 b,d,f. The analysis graphs for the spots shown in Figures 93 b,d,f are given in Figures 94, 95, and 96, respectively. As can be observed in these analyses, the data indicate that cobalt was excluded from the intracrystalline zeolite pore system but that thoria was present in small amounts internally. The crystals shown in Figures 93 d and f are the same crystal at two different orientations with respect to the electron beam. It can be seen that at least 30 microns of ZSM-5 depth were below the spots taken at the location shown in Figure 93 f. This massive depth below the analysis spot insured the tear drop shape analysis volume did not detect metals occurring on the far surface of the zeolite crystal. The absence of the gold peak also supported this fact. It was clear that crystals of this size were extremely useful in determining the extent of metal transport into the zeolite pore system during impregnation.

The final objective of the synthesis effort was to attempt to incorporate transition metals into the zeolite pore system by occlusion during synthesis. Restricted transition state selectivity which prevents the formation of polyaromatic rings inside the ZSM-5 pore system would make such occluded metals immune to coking. Cscseri[126] discussed the formation of coke in zeolites and pointed out that although coke can form in the large port zeolites such as mordenite, it can only form on the surface of Pentasil zeolites. The diagram he presented is shown in Figure 97.[126] Table 28 in Appendix D shows the various systems investigated in attempt to occlude transition metals within the ZSM-5 pore system. It was found that the hydrothermal synthesis of ZSM-5 was possible in the presence of the high valence hydroxides of iron, nickel, copper, chromium, platinum, palladium, rhodium, ruthenium, cobalt, and tin. The presence of the transition metal hydroxides did not impede the crystallization of ZSM-5 for all metals mentioned except ruthenium, chromium and cobalt. The x-ray diffraction analysis of each of the products for the hydrothermal synthesis listed in Appendix D, Table 28, is provided in Appendix E. Each of these synthesis was carried out under autogenous pressure in a 2 liter Parr autoclave. Scanning electron micrographs of the products formed are given in Figures 98, 99, and 100. Figure 98 shows the crystal morphology formed in the presence of Rh and Pt, Figure 99 that for Sn, Ru, and Pt, and Figure 100 the morphology formed in systems containing Fe, Ru, and Ni. In general, the crystals were speckled with amorphous clumps of the metal oxides. Electron microprobe analysis showed high concentrations of the transition metal and the surface of the crystals also showed substantial concentrations of the specific transition metal. Microprobe analysis by transmittence electron microscopy on DOD-Fe-ZSM-5-1 showed the silicon to iron ratio to vary from 40:1 to 3200:1. The aluminum to iron ratios varied from 1.6:1 to 60:1. The thin section observed was fractured from the inside of a ZSM-5 crystal. The presence of iron indicated the likelihood that this metal was being occluded during synthesis and the fact the aluminum to iron ratio varied suggested it might not be present simply as a cation bouncing the negative charge on the aluminum. The color of the occluded iron was purple and it is, therefore, likely to be present as the $Fe(H_2O)_6$ or $Fe(NH_4)_6$. To determine if iron was being incorporated in the lattice by salt occlusion or simply by ion-exchange during synthesis, the synthesis of silicalite was carried out in the presence of ferric hydroxide. The crystals formed were pink-purple in color and since no aluminum was present in the framework, it is probable that the metal is being occluded as a complete salt. Mossbauer analysis showed the iron to be 85% superparamagnetic which is considerably higher than the degree of super paramagnetism found in samples impregnated using the carbonele method of impregnation. The Mossbauer results suggest that the iron is at its high spin electron configuration having 5 unpaired electrons. 5 unpaired electrons are likely to give rise to outstanding catalytic activity. Much work is left to determine the extent of metal inclusion in the other samples synthesized.

Figure 91. Various Crystal Morphologies Obtained in Systems Containing Ammonia

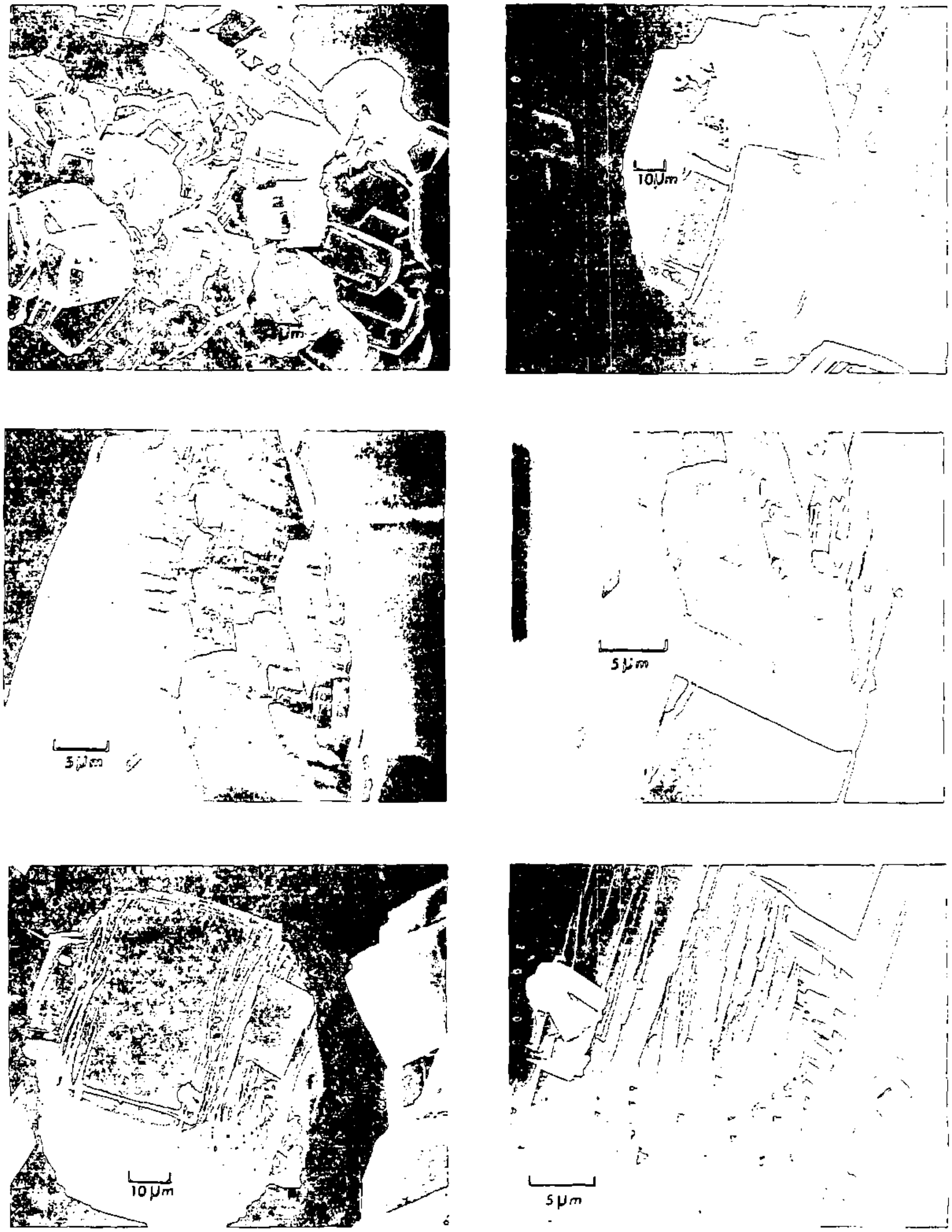

Figure 92. a,b,c,e,f. Incipient wetness, Aqueous
Iron nitrate Impregnation of
large ZSM-5 crystals

Figure 92. d. Back Scatter Electron Image Showing The
Location of Iron Atoms.

Figure 92 a

Figure 92 b

Figure 92 c

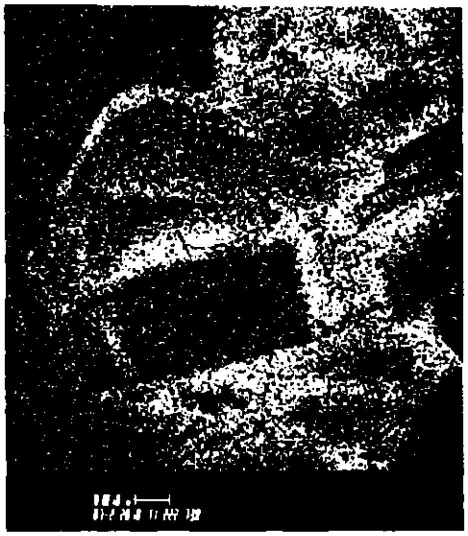

Figure 92 d

Figure 92 Continued

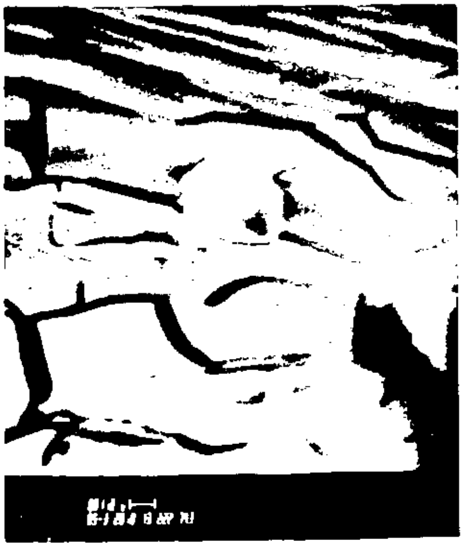

Figure 92 e

Figure 92 f

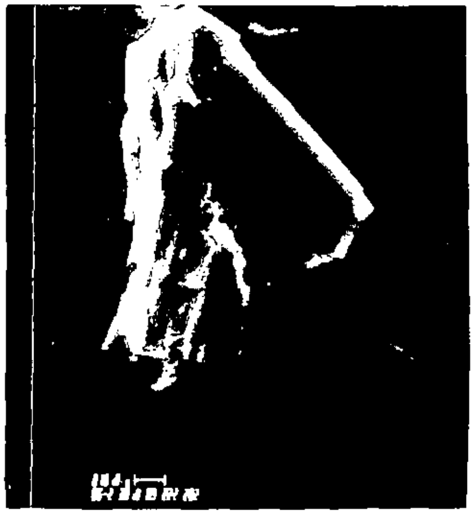

Figure 93 a

Shows cobalt thoria impregnated silicalite single crystal. Impregnation solution composition 15.26 gms Co $(NO_3)_2 \cdot 6\ H_2O$, 1.03 gms Th $(NO_3)_4 \cdot 4\ H_2O$ per 500 ml acetone at 120 C. Crystal has fractured surface exposed.

Figure 93 b

Higher magnification of crystal in 93a Spots a - g and field h given in analyses 11 through 18.

Figure 93 c

Cobalt thoria impregnated silicalite. Impregnation temperature 120 C and solution composition 15.26 gms Co $(NO_3)_2 \cdot$ 6 $H_2O$, 1.03 gms Th $(NO_3)_4 \cdot 4\ H_2O$ per 50 ml acetone.,

Figure 93 d

Close-up of 93c showing fractured crystal surface. Analysis of spots a-g (excluding e) appear in analyses 19 through 24.

Figure 93 e

Shows same silicalite crystal as in Fig 93 d. at a different orientation.

Figure 93 f

Shows back scatter image of same crystal as in Fig 93 a and e Analysis of spots a-h appear in analyses 25-32. Comparing this fractured surface to SEM given in 24, one can see there is at least 20 microns of depth below these analyses spots. Since the maximum tear drop depth below the analysis beam is 6 microns, we can be assured we're not observ-the metals on the far side of the crystal.

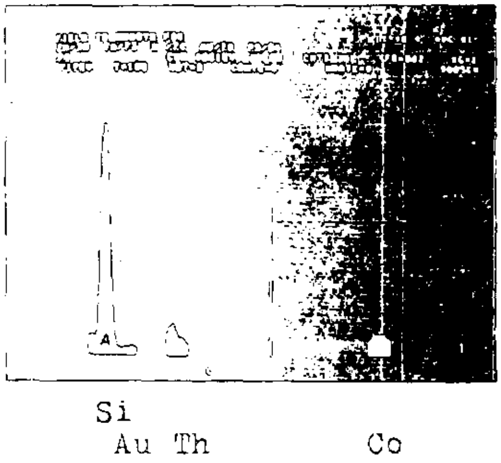

Figure 94 a
Analysis of spot A in 93b shows higher level of thorium than cobalt on fractured surface.

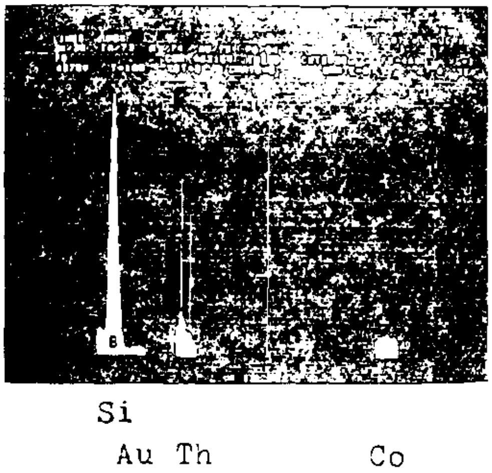

Figure 94 b
Analysis of spot B of fractured surface of crystal in 93b shows higher level of thorium than cobalt.

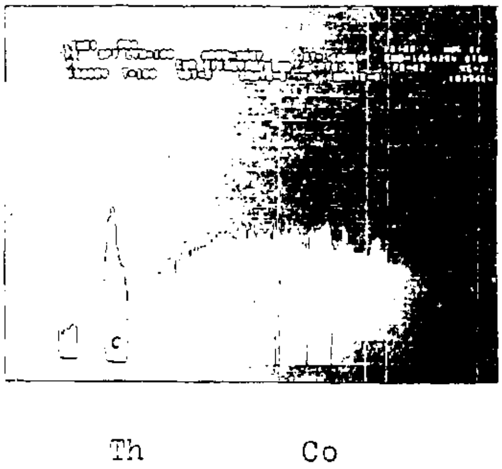

Figure 94 c
Analysis of spot C on crystal in 93b shows higher level of thorium than that of cobalt inside crystal.

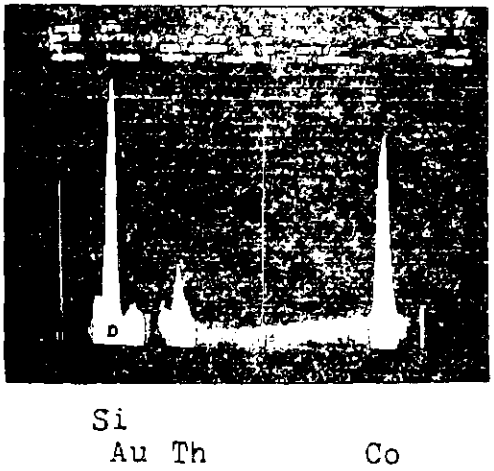

Figure 94 d
Analysis of spot D on crust covering outer surface of crystal in 93b shows it to contain a high level of cobalt.

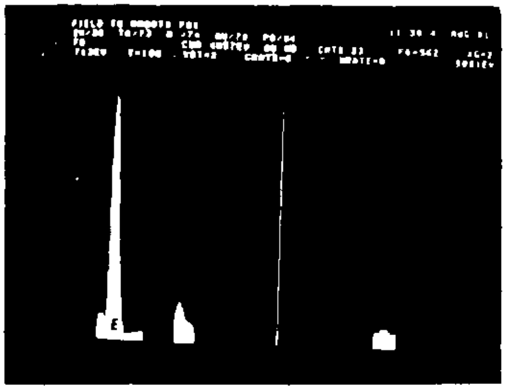

Figure 94 e
Analysis of spot E on crystal in 93b indicates thorium has moved all the way to the center of the crystal.

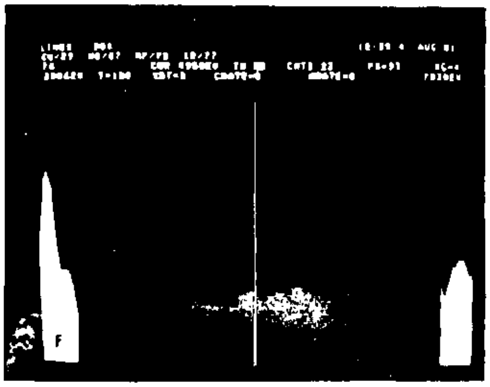

Figure 94 f
Analysis of spot F inside crystal shown in 93b shows a higher relative level of thorium to that of cobalt.

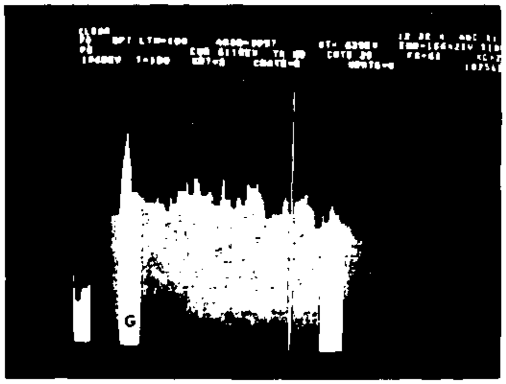

Figure 94 g
Analysis of spot G on fractured surface of crystal in 93b shows thorium is present and cobalt is absent.

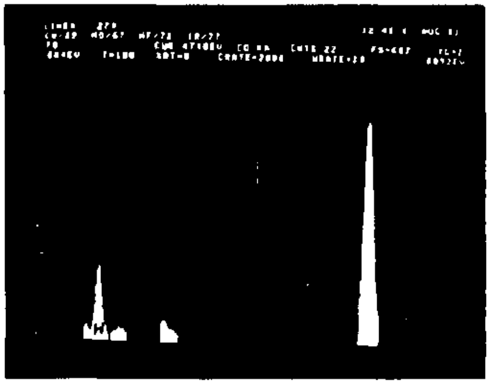

Figure 94 h
Analysis of spot H of crust covering crystal in 93b shows it to be predominately cobalt.

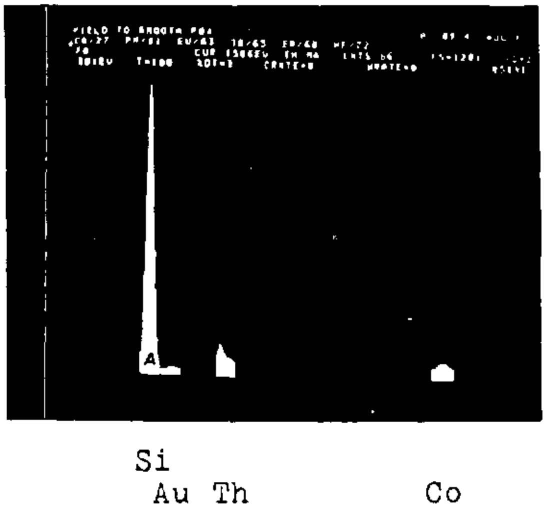

Figure 95 a
Analysis of spot A on 93 d shows relative level of thorium over cobalt inside crystal.

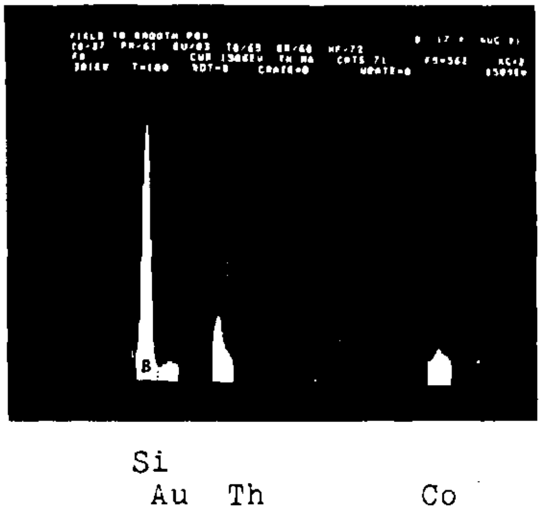

Figure 95 b
Analysis of spot B on 93 d shows relative level of thorium over cobalt inside crystal.

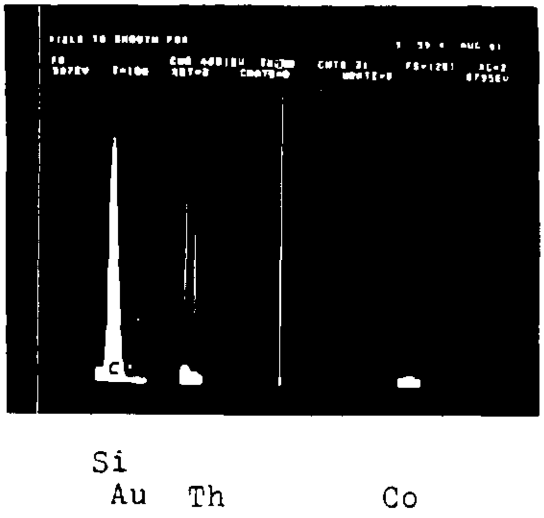

Figure 95 c
Analysis of spot C on 93 d shows relative level of thorium over cobalt inside crystal.

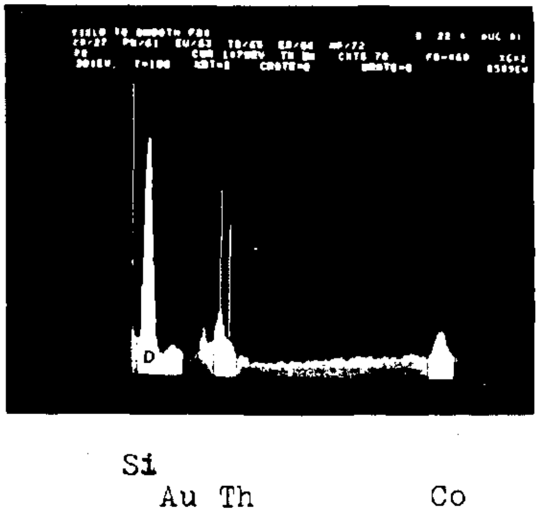

Figure 95 d
Analysis of spot D on 93 d shows a higher level of thorium than that of cobalt inside the crystal.

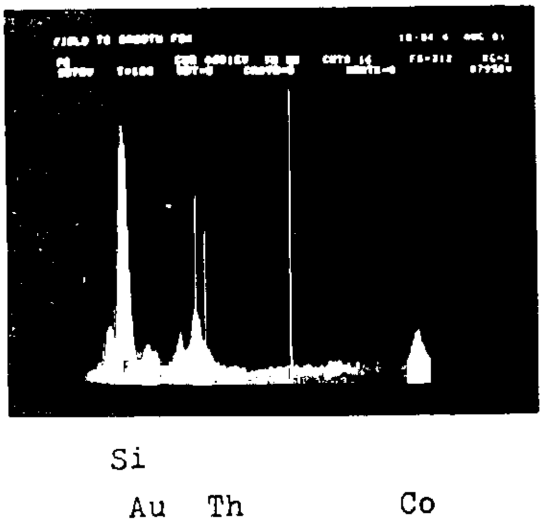

Figure 95 e
Analysis of spot F just inside fracture of the crystal in 93d shows that although, the thorium level is still dominant, cobalt is higher near crystal surface.

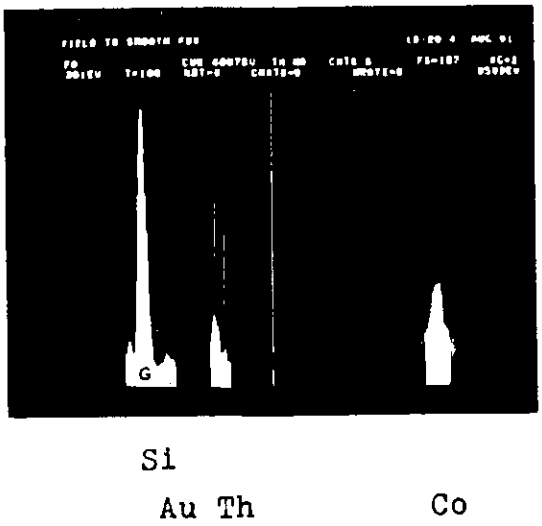

Figure 95 f
Analysis of spot G in 93 d shows cobalt intensity higher on surface.

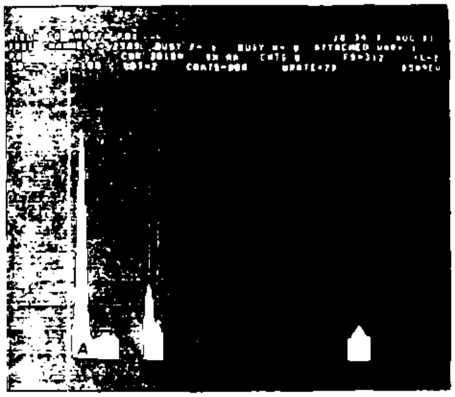

Figure 96 a
Analysis of spot A in 93f . shows the relative intensity of thorium to be higher than cobalt on this fractured surface. Gold peak is absent indicating we are observing the inside of this crystal

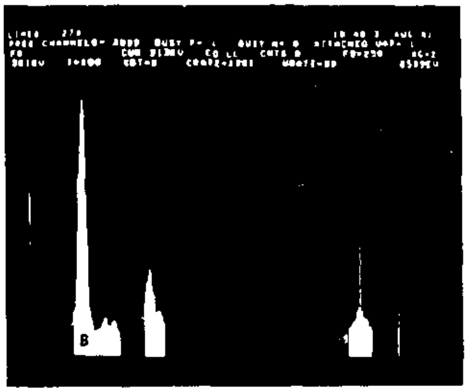

Figure 96 b
Analysis of spot B on fractured surface of crystal in 93 f . The relative intensity of thorium is higher than that of cobalt.

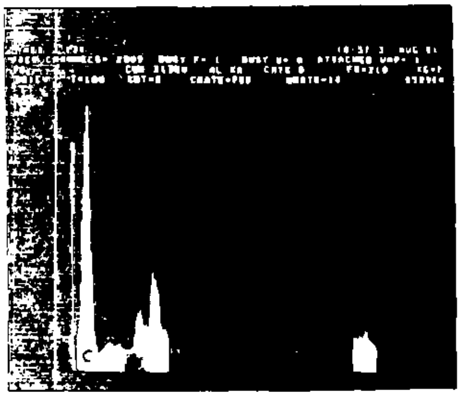

Figure 96 c
Analysis of spot C on fractured surface of crystal in 93f shows a substantially higher level of thorium to that of cobalt.

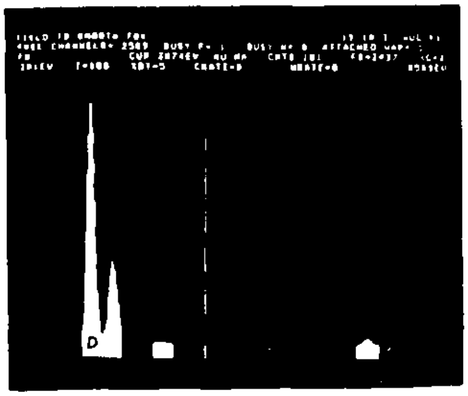

Figure 96 d
Analysis of spot D on surface of crystal in 93 f shows gold peak indicating that this is an original (non fractured) surface.

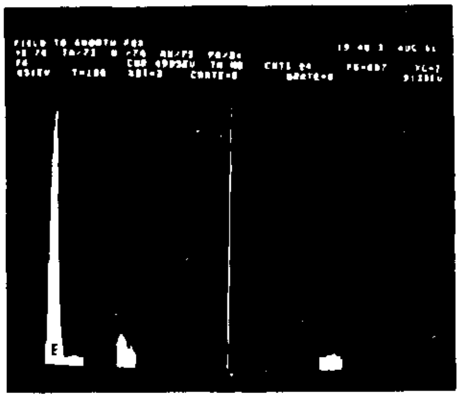

Figure 96 e

Analysis of spot E on fractured surface of 93 f shows a slightly higher level of thorium relative to cobalt.

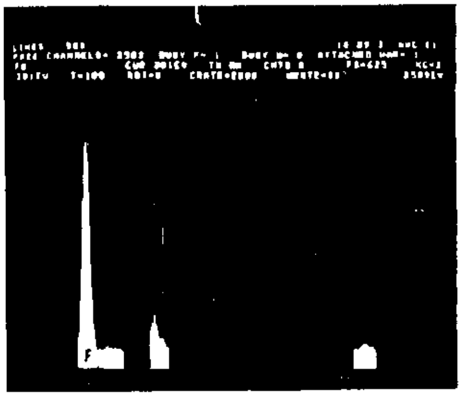

Figure 96 f

Analysis of spot F on fractured surface of crystal in 93f shows a higher level of thorium than cobalt.

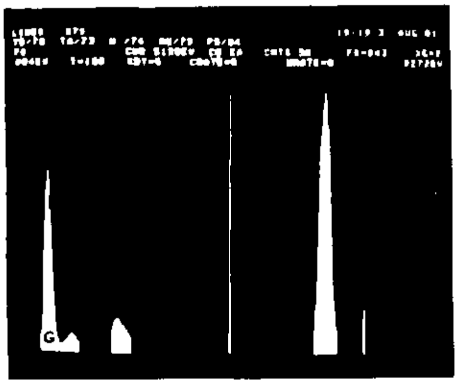

Figure 96 g

Analysis of spot G on crusty material adhering to crystal in 93 f shows it to consist predominately of cobalt.

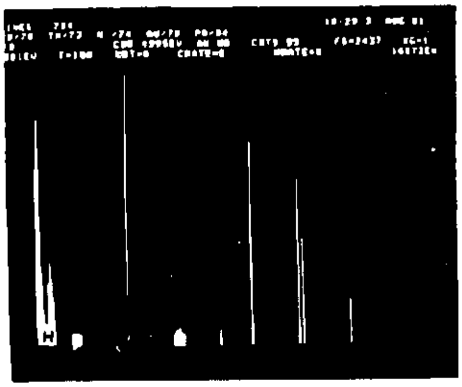

Figure 96 h

Analysis of region H on outer surface of crystal on 93 f shows a high gold level, indicating it is a non-fractured surface.

Figure 97. COKE FORMATION IN ZEOLITES

A. Pentasil Zeolites

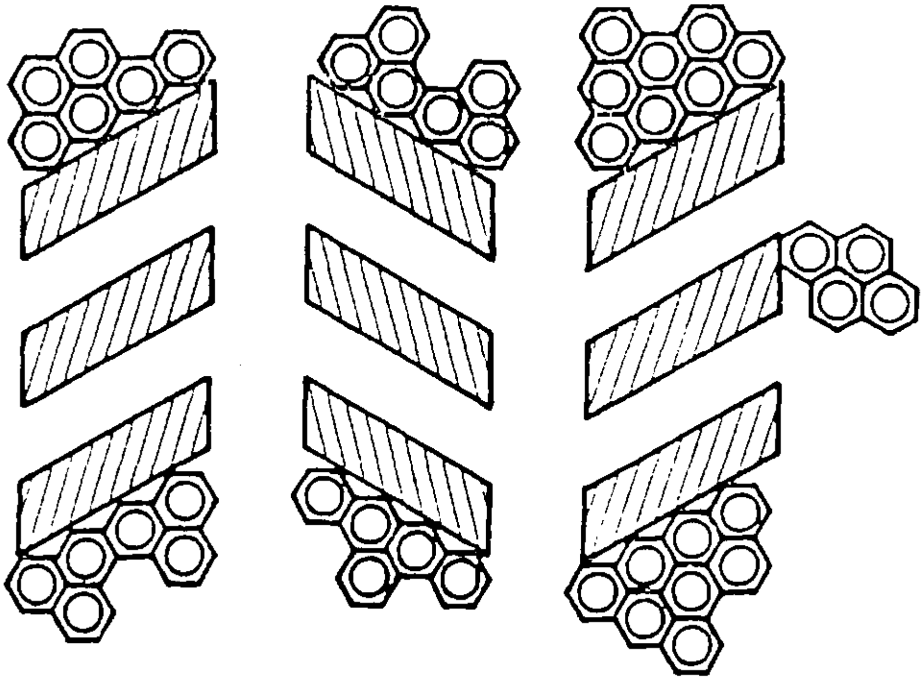

B. Mordenite (and Other Large Pore Zeolites)

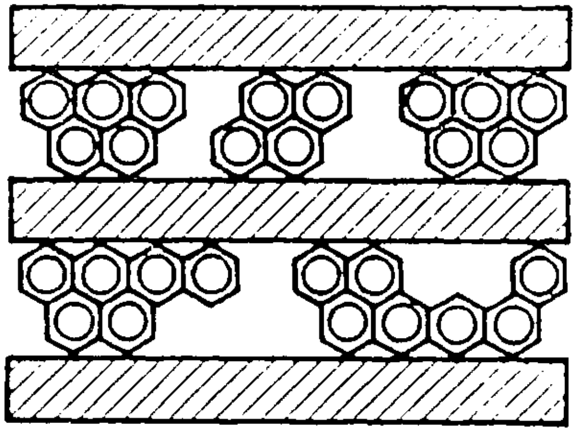

Dejaifve, et al., J. Catal., 70, 123 (1981).[126]

DOD-Rh-ZSM-5-12-21-82

Figure 98 a

DOD-Rh-ZSM-5-12-21-82

Figure 98 b

DOD-Rh-ZSM-5-1-11-15

Figure 98 c

DOD-Rh-ZSM-5-2-11-80

Figure 98 d

DOD-Pt-ZSM-5-1-11-12

Figure 98 e

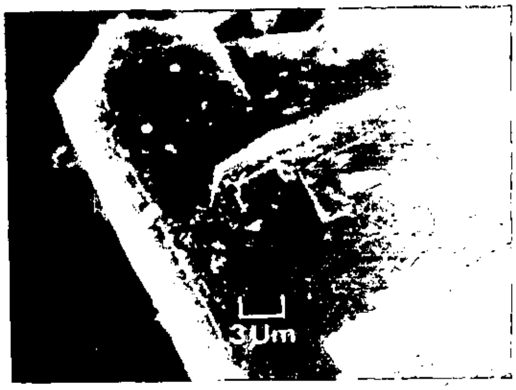

DOD-Pt-ZSM-5-1-11-12

Figure 98 f

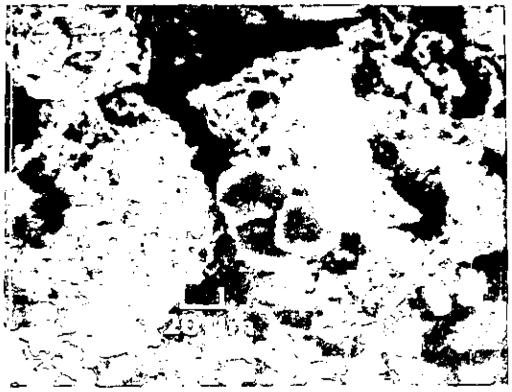

DOD-Pt-ZSM-5-3.6

after calcination and ion-exchange

Figure 98 g

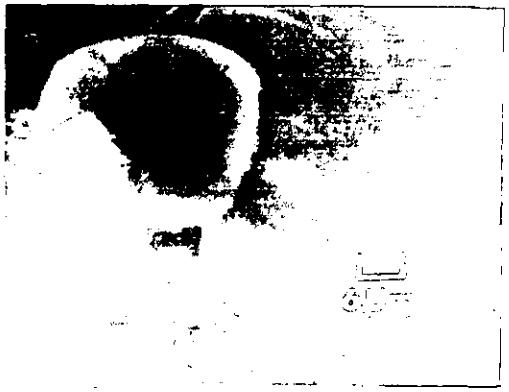

DOD-Pt-ZSM-5-3.6

after calcination and ion-exchange

Figure 98 h

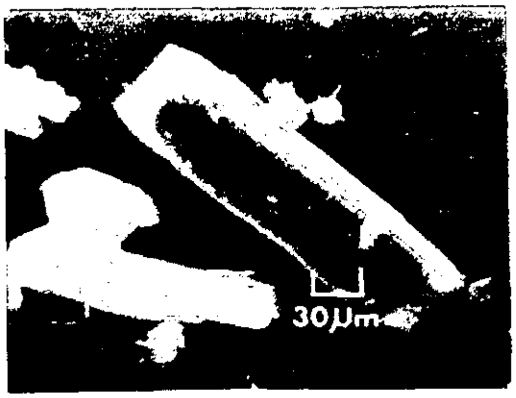

DOD-Pt-ZSM-5-1-11-12

Figure 99 a

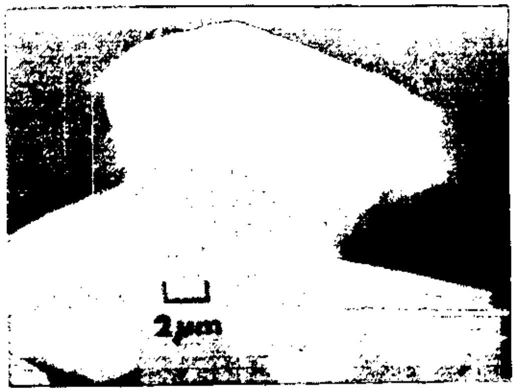

DOD-Pt-ZSM-5-1-11-12

Figure 99 b

DOD-Pt-INS-ZSM-5-1

Figure 99 c

DOD-Pt-ZSM-5-3.6

Figure 99 d

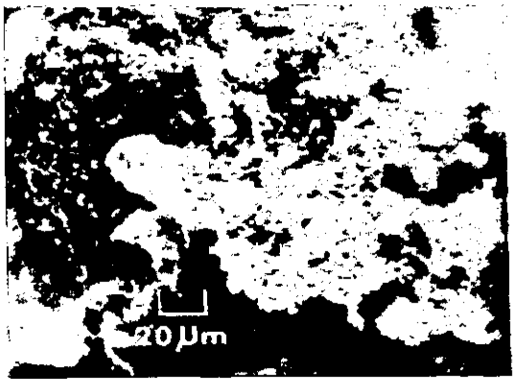

DOD-SN-ZSM-5-1-12-3

Figure 99 e

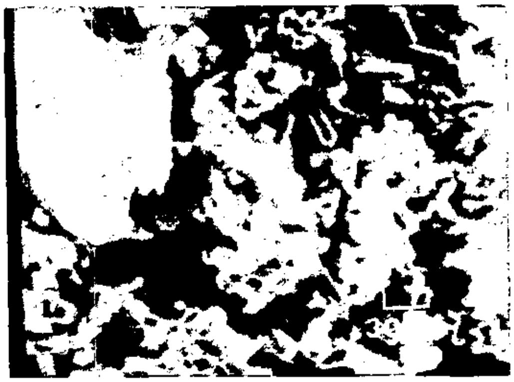

DOD-Pt-ZSM-5-1-11-12

After calcination and

ion-exchange

Figure 99 f

DOD-Ru-ZSM-5-1-11-29

Figure 99 g

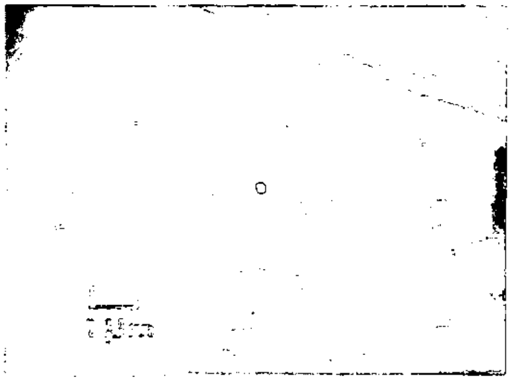

DOD-Ru-ZSM-5-1-11-29

Figure 99 h

DOD-Fe-ZSM-5-3

Figure 100 a

DOD-Fe-ZSM-5-3

Figure 100 b

DOD-Fe-ZSM-5-5

Figure 100 c

DOD-Fe-ZSM-5-5

Figure 100 d

DOD-Ru-ZSM-5-1-11-29

Figure 100 e

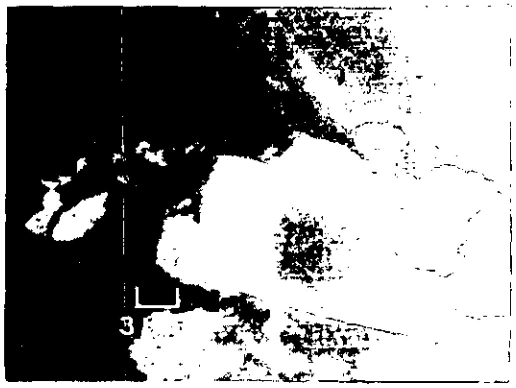

DOD-Ni-ZSM-5-2-11-12

Figure 100 f

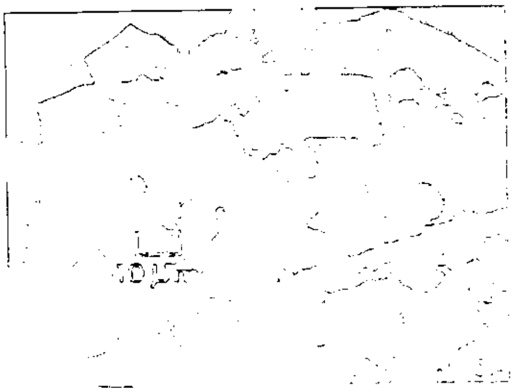

DOD-Ru-ZSM-5-1-11-29

Figure 100 g

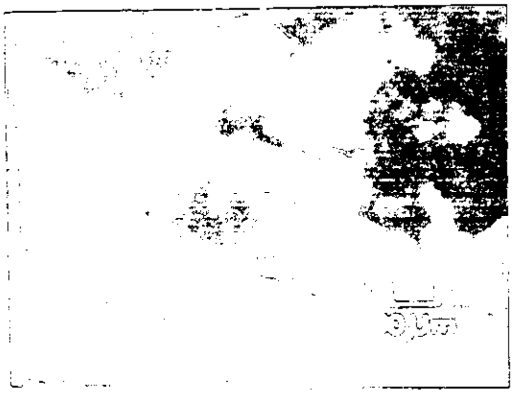

DOD-Ni-ZSM-5-2-11-12

Figure 100 h